

Experimental and numerical investigation of temperature distribution and melt pool geometry during pulsed laser welding of Ti6Al4V alloy



Mohammad Akbari ^{a,*}, Seyfolah Saedodin ^a, Davood Toghraie ^b,
Reza Shoja-Razavi ^c, Farshad Kowsari ^d

^a Department of Mechanical Engineering, Semnan University, Semnan, Iran

^b Department of Mechanical Engineering, Islamic Azad University, Khomeinshahr branch, Isfahan, Iran

^c Department of Materials Engineering, Malek-Ashtar University of Technology, Shahinshahr, Isfahan, Iran

^d Department of Mechanical Engineering, Tehran University, Tehran, Iran

ARTICLE INFO

Article history:

Received 3 September 2013

Received in revised form

13 December 2013

Accepted 14 December 2013

Available online 4 January 2014

Keywords:

Titanium alloy

Laser welding

Temperature distribution

ABSTRACT

This paper reports on a numerical and experimental investigation of laser welding of titanium alloy (Ti6Al4V) for modeling the temperature distribution to predict the heat affected zone (HAZ), depth and width of the molten pool. This is a transient three-dimensional problem in which, because of simplicity, the weld pool surface is considered flat. The complex physical phenomenon causing the formation of keyhole has not been considered. The temperature histories of welding process were studied. It was observed that the finite volume thermal model was in good agreement with the experimental data. Also, we predicted the temperature as a function of distance at different laser welding speeds and saw that at each welding speed, the temperature profile was decreased sharply in points close to the laser beam center, and then decreased slightly in the far region from the laser beam center. The model prediction error was found to be in the 2–17% range with most numerical values falling within 7% of the experimental values.

© 2013 Elsevier Ltd. All rights reserved.

1. Introduction

High power density welding processes are able to operate in a mode in which they can penetrate thicker workpieces with a single pass and produce welds with a high ratio of penetration to width. The increased interest by industry in laser welding is because this technique has shown high efficiency and low production cost compared to other welding methods. Several techniques have been considered to achieve reliable welds with minimum distortion for the fabrication of components in different industries. Of these methods, laser welding can provide a significant benefit for the welding because of its precision and rapid processing capability. This technique is finding applications in aerospace, automotive, pressure vessels, etc. During the laser welding some sequential types of the phase transitions such as alpha-beta titanium transformation in the solid phase, melting, evaporation, ionization occur and then in the reverse order during cooling stage. There are two types of lasers: continuous wave (CW) and pulsed wave (PW). The welding parameters normally associated with CW lasers are laser power, beam diameter and welding speed. In PW lasers, the parameters used are pulse duration, energy and beam diameter.

The difficulties in directly comparing these two types of lasers are due to the parameters utilized. In a detailed review paper, Mackwood and Crafer [1] emphasized on thermal modeling and prediction of laser welding and similar techniques were employed to model conventional welding processes such as arc, resistance and friction as well as related processes such as alloying, cladding and surface hardening in metals. The time frame of their review was up to the year 2002.

Titanium and its alloys have been widely used due to low density, good corrosion resistance, high operating temperature, etc. Some applications of titanium alloys in aerospace, biomedical, nuclear and automotive industries are reported by Wang et al. [2] and Casalino et al. [3]. Ti6Al4V is the most famous titanium alloy which, because of high strength, low thermal conductivity and high chemical reactivity, has difficult conventional machining and welding. Laser is used to solve this problem. Also, Ti6Al4V can be welded using a PW and CW laser. Several studies on the effect of different welding parameters in laser welding of Ti6Al4V have been conducted experimentally and numerically.

Joining Ti6Al4V titanium alloys using pulsed Nd:YAG laser welding method was done by Akman et al. [4]. Their results showed that it was possible to control the penetration depth and geometry of the laser weld bead by precisely controlling the laser output parameters. Blackburn et al. [5] produced the welds with high internal quality in Ti6Al4V up to 3.25 mm in thickness by

* Corresponding author.

E-mail address: m.akbari.g80@gmail.com (M. Akbari).

Nomenclature		x, y, z	coordinates (m)
c_p	specific heat capacity ($\text{J kg}^{-1} \text{K}^{-1}$)	Greek symbols	
h_{ext}	convective heat transfer coefficient ($\text{W m}^{-2} \text{K}^{-1}$)		
k	thermal conductivity ($\text{W m}^{-1} \text{K}^{-1}$)	α	absorption coefficient
K	permeability (m^2)	β	volumetric thermal expansion coefficient (K^{-1})
P	total power of the laser beam (W)	ΔH	latent heat of fusion (J kg^{-1})
q	convective heat flux (W)	ε	emissivity coefficient
S	heat source (W m^{-3})	η	average absorptivity coefficient
u, v, w	velocity components (ms^{-1})	μ	dynamic viscosity ($\text{kg m}^{-1} \text{s}^{-1}$)
T	temperature (K)	ρ	density (kg m^{-3})
T_{ext}	ambient temperature (K)	γ	coefficient of surface tension (J m^{-2})
T_w	welding temperature (K)		
v_{welding}	velocity of the workpiece (ms^{-1})		

using laser source as a welding technique. They observed the common periodic behaviors in the vapor plume and keyhole in low porosity welding conditions. Comparison of the properties of the Ti6Al4V titanium alloy joints with pulsed Nd:YAG laser welding and gas tungsten arc welding was made by Gao et al. [6]. They concluded that because the samples welded by laser beam welding had small residual distortions and narrow HAZ, fine microstructures and high Vickers hardness pulsed Nd:YAG laser welding was better than gas tungsten arc welding. Yang et al. [7] provided a finite element model to predict the depth and width of HAZ in laser heating of Ti6Al4V alloy plate and found that the depth and width of HAZ were decreased with an increase of laser scan speed.

There are several experimental and numerical studies on the effect of different welding parameters in laser welding of other materials. For example, Kong et al. [8] developed a model based on a double-ellipsoidal volume heat source to simulate the gas metal arc welding of ASTM A36 carbon steel and a cylindrical volume heat source to simulate the laser beam. They concluded that the proposed model could be further applied to the optimization of the processing parameters of hybrid laser–gas metal arc welding as well as other welding methods.

Frewin and Scott [9] produced a time-dependent 3D model of heat flow during pulsed Nd:YAG laser welding. By ignoring the convective flows in the melt pool and assuming a Gaussian energy distribution, they calculated transient temperature cross-sections along with the dimensions of the fusion and HAZ. They found that the fusion and HAZ produced numerically were extremely close to those produced experimentally. Semak et al. [10] produced a laser welding model based on a hydrodynamic physical model of laser–material interaction including the effect of evaporation recoil pressure and convection on melt flow. Their simulations showed that convective heat transfer induced by recoil pressure was significant at intensities corresponding to laser welding, cutting, and drilling due to melt ejection. They also showed that motion in the molten zone outwards from the beam resulted in a secondary temperature maximum. They also reported that maximum penetration was dependent on the specific location of the beam focus [11]. A 3D finite element model to simulate the laser welding process of AA5083 thin sheets was presented and carried out by Spina et al. [12]. The usefulness of the finite element model for modeling laser welding and prediction of displacements of specimens in different welding speeds were observed in their simulation. The martensite decomposition in the HAZ was considered under various temperature gradients by Kovacevic et al. [13]. They observed the finer mean grain size of martensite and the smaller percentage of martensite decomposition with the increase in scanning speed. The prediction of temperature distributions and the effect of variations in absorption

coefficient, thermophysical properties and gas shielding on the width and depth of melt pool and temperature distributions were investigated by Bannour et al. [14]. Their results showed that the weld pool shape and temperature distribution are highly affected by absorption coefficient and the thermal conductivity. Also, the molten pool shape becomes wider and deeper when these parameters vary with temperature. Using nanosecond pulsed laser, Fortunato et al. [15] presented a numerical simulation of micro-welding and predicted the dimensions of weld pool and the heat-affected zone. The obtained parameters were successfully applied in the welding of a 1%C shaft and a 0.7%C gear and there was no variation of the micro-hardness in the heat-affected zone. Assuncao and Williams [16] compared the PW laser and CW laser welds. Their results showed that the two lasers had very dissimilar behaviors in terms of penetration depth. Also, the PW laser showed higher efficiency under the same welding conditions. The possibility of constructing a parameter space for the prediction of weld properties was studied using weld cross section measurements by Zervaki et al. [17]. Presenting a correlation for hardness based on the temperature and understanding the mechanisms occurring during welding process were the key findings of their work.

Review of aforementioned articles and other related Refs. [18–21] showed that various parameters were investigated in different studies. From each work, different aspects of laser welding were studied and therefore, different results were obtained, each of which could be useful in its position. However, no comprehensive study in these research fields was found to predict the width and depth of molten pool by using temperature history. Therefore, it seems that more research can make a good contribution to the removal of shortcomings in other works. We have carried out a numerical and experimental study of laser welding for modeling of temperature distribution and molten pool shape to predict the depth and width of the molten pool and HAZ dimensions. The objective of this paper was to examine the effect of welding speed on the temperature distribution, weld depth and weld width. The obtained results showed that this study could help understand the mechanism of laser welding better.

2. Experimental procedure

Experiments were performed to characterize the temperature measurements and HAZ dimensions in laser welding. The sample was Ti6Al4V alloy plate (50 mm \times 20 mm with the thickness of 3 mm). The chemical composition of Ti6Al4V alloy (in wt%) is given in Table 1.

A model IQL-20 pulsed Nd:YAG laser with a maximum mean laser power of 750 W and wavelength 1.06 μm was used as the laser source. The laser parameter ranges were 0.2–25 ms for pulse duration,

Table 1
Chemical composition of Ti6Al4V as mass percentage.

Al%	V%	Cr%	Cu%	Fe%	Mn%	Mo%	Nb%	Sn%	Zr%	Si%	Ti%
6.5	4.0	< 0.01	< 0.02	0.04	0.02	< 0.03	0.02	< 0.05	0.02	0.03	Base

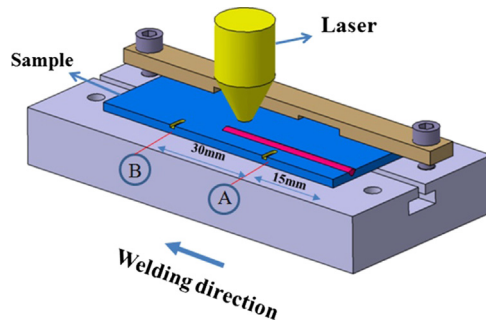


Fig. 1. A schematic illustration of the laser welding experiment.

1–250 Hz for pulse frequency and 0–40 J for pulse energy. The spot diameter on the surface of the plate was set at about 0.7 mm. A W-Lp 400 Ophir power meter was used to measure the average power. The temporal shape of the laser output pulses was like a square. The focal point was 6 mm above the surface of the workpiece. For the purpose of shielding, the pure argon gas from a coaxial nozzle was used with the flow rate at 15 l/min. Fig. 1 shows a schematic illustration of the experimental setup.

K-type thermocouples with an operative range between -40°C and $+1260^{\circ}\text{C}$ and the accuracy between $\pm 1\%$ were used for temperature measurement. Because the temperature of the molten pool was very high, the thermocouples were attached on the top surface at 2 mm lateral distance from the center of the molten pool. The locations of thermocouples are specified in Fig. 1 (points A and B). The workpieces were polished completely and laser welding (with 240 W mean laser power, 4.2 ms pulse duration, 25 Hz frequency and different welding speeds) was performed. The data were recorded using the data acquisition card (model: Advantech USB 4718). For the metallographic preparation, all the samples were mounted, polished using the standard metallographic techniques (200,400, 600, 800 and 1000 grit) and etched using Kroll's reagent (Distilled water-92 ml, nitric acid-6 ml and hydrofluoric acid-2 ml). The width and depth of the molten pool were measured using an Olympus SZ-X16 stereoscopic microscope.

3. Numerical simulation

The geometrical configuration of the problem in the Cartesian coordinates system is shown in Fig. 2.

The purpose of this study was the numerical modeling and experimental investigation of temperature distribution and molten pool dimensions to predict the depth and width of the molten pool and HAZ dimensions. Due to the fact that the workpiece is moving in x direction, the temperature distribution and the melting pool shape are not asymmetric. As a result, the problem is a transient three-dimensional problem. For simplicity, the weld pool surface was considered to be flat and the complex physical phenomenon causing the formation of keyhole was not considered.

The calculation domain was $50\text{ (mm)} \times 20\text{ (mm)} \times 3\text{ (mm)}$ (length \times width \times thickness). This domain was divided into a non-uniform grid system for the weld pool in which a finer mesh was located at the weld zone in order to ensure enough numerical precision and the courser mesh was used at the area far from the weld zone in order to reduce the computation cost. The governing

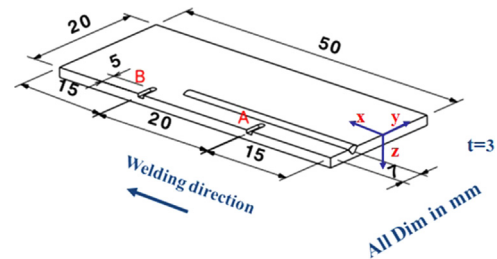


Fig. 2. Schematic model for laser welding.

equations and their boundary conditions were discretized by control volume schemes. The SIMPLE algorithm and first upwind discretization method [22] were used to calculate the fluid flow and heat transfer phenomena. The grid space used for the weld zone was 0.25 mm in x , y and z directions and at the area far from the weld zone, it was 1.25 mm in x , y and z directions. In order to improve the accuracy of the calculation, $195 \times 50 \times 8$ grids were used for the weld zone and $41 \times 16 \times 3$ grid were used for area far from the weld zone. The fixed time step (0.00001 s) was used in the whole computation. Also, calculation of solid and liquid regions was performed using the enthalpy method.

3.1. Governing equations

- The mathematical formulation of the model is based on the following assumptions:
- The initial temperature for workpiece is at 293 K.
- The laser beam and coordinate system are fixed.
- The workpiece moves in the x -direction with a constant velocity, v_{welding} .
- The surface of weld pool is flat.
- All thermophysical properties of the material are temperature dependent.
- In the melt pool, the fluid flow is laminar and incompressible.
- The flow is transient.

In this study, the convective heat transfer in the molten zone and the influence of laser welding speed on the weld pool shape and size were investigated. Also, by using laminar pattern approximation, we could reduce the simulation to the heat transfer in the liquid and solid phases. Momentum and energy equations had to be coupled to determine the temperature and velocity distribution. The equations of continuity, energy and momentum in the Cartesian coordinate system can be written as follows [23]

Continuity equation:

$$\frac{\partial \rho}{\partial t} + \frac{\partial(\rho u)}{\partial x} + \frac{\partial(\rho v)}{\partial y} + \frac{\partial(\rho w)}{\partial z} = 0 \quad (1)$$

X-momentum equation:

$$\begin{aligned} \frac{\partial(\rho u)}{\partial t} + \frac{\partial(\rho uu)}{\partial x} + \frac{\partial(\rho uv)}{\partial y} + \frac{\partial(\rho uw)}{\partial z} \\ = -\frac{\partial P}{\partial x} + \frac{\partial}{\partial x} \left(\mu \frac{\partial u}{\partial x} \right) + \frac{\partial}{\partial y} \left(\mu \frac{\partial u}{\partial y} \right) + \frac{\partial}{\partial z} \left(\mu \frac{\partial u}{\partial z} \right) - \frac{\mu}{K} (u - v_w) \end{aligned} \quad (2)$$

Y-momentum equation:

$$\frac{\partial(\rho v)}{\partial t} + \frac{\partial(\rho v u)}{\partial x} + \frac{\partial(\rho v v)}{\partial y} + \frac{\partial(\rho v w)}{\partial z} = -\frac{\partial P}{\partial y} + \frac{\partial}{\partial x} \left(\mu \frac{\partial v}{\partial x} \right) + \frac{\partial}{\partial y} \left(\mu \frac{\partial v}{\partial y} \right) + \frac{\partial}{\partial z} \left(\mu \frac{\partial v}{\partial z} \right) - \frac{\mu}{K} v \quad (3)$$

Z-momentum equation:

$$\frac{\partial(\rho w)}{\partial t} + \frac{\partial(\rho w u)}{\partial x} + \frac{\partial(\rho w v)}{\partial y} + \frac{\partial(\rho w w)}{\partial z} = -\frac{\partial P}{\partial z} + \frac{\partial}{\partial x} \left(\mu \frac{\partial w}{\partial x} \right) + \frac{\partial}{\partial y} \left(\mu \frac{\partial w}{\partial y} \right) + \frac{\partial}{\partial z} \left(\mu \frac{\partial w}{\partial z} \right) - \frac{\mu}{K} w + \rho g \beta (T - T_{\text{ref}}) \quad (4)$$

Energy equation:

$$\rho C_p \left(\frac{\partial T}{\partial t} + (u - v_w) \frac{\partial T}{\partial x} + v \frac{\partial T}{\partial y} + w \frac{\partial T}{\partial z} \right) = \frac{\partial}{\partial x} \left(k \frac{\partial T}{\partial x} \right) + \frac{\partial}{\partial y} \left(k \frac{\partial T}{\partial y} \right) + \frac{\partial}{\partial z} \left(k \frac{\partial T}{\partial z} \right) + S - \frac{\partial}{\partial x} (\rho u \Delta H) - \frac{\partial}{\partial y} (\rho v \Delta H) - \frac{\partial}{\partial z} (\rho w \Delta H) \quad (5)$$

In momentum equations, K is the permeability coefficient, which is related to the liquid volume fraction with the Koreny–Carman equation [24]. It enables us to have a smooth transition of velocity from zero in the solid region to a large value in the fully liquid region for the fixed-grid numerical method [25]. In energy equation, according to a suitable latent updating form during each interaction within a time step updated, a source-based method is used to deal with the latent heat of fusion, ΔH , as an additional heat source. By introducing the permeability factor and source-based method, Eqs. (1)–(5) are unique for both liquid and solid phases. Therefore, it is not necessary to track the melt–solid interface and specify a boundary at that location. In the weld pool, the surface tension force, the Lorentz force and the buoyancy force interact with each other. The Marangoni convection which is the main driving force of the fluid flow, acts because of the temperature dependence of the surface tension [26,27]. The boundary conditions at the upper surface are as follows:

For the weld pool (in the liquid region)

$$\mu \frac{\partial u}{\partial z} = -\frac{\partial \gamma}{\partial T} \frac{\partial T}{\partial x}; \quad \mu \frac{\partial v}{\partial z} = -\frac{\partial \gamma}{\partial T} \frac{\partial T}{\partial y}; \quad w = 0 \quad (6)$$

where $(\partial \gamma / \partial T)$ is the temperature coefficient of surface tension.

For the solid region

$$u = v_{\text{welding}}; \quad v = 0; \quad w = 0 \quad (7)$$

3.2. Boundary and initial conditions

The initial condition at time $t=0$ is given as

$$T(x, y, z, 0) = 0 \quad (8)$$

The convection and radiation boundary conditions on all surfaces are considered. In addition, on the top surface, a transient heat flux (which is produced by the beam laser) is considered.

$$\text{for } z=0 \quad -k \frac{\partial T}{\partial z} = q - \varepsilon(T) \sigma (T^4 - T_{\infty}^4) - h(T - T_{\infty}) \quad (9)$$

where h is the convective heat transfer coefficient, σ is Stefan–Boltzmann constant $= 5.67 \times 10^8 \text{ W/m}^2 \text{ K}^4$ and ε is emissivity. For radiation and convection problems, the following lumped convection coefficient was used as suggested by Frewin and Scott [9]

$$h = 2.4 \times 10^{-3} \varepsilon T^{1.61} \quad (10)$$

Note that the temperature-dependent emissivity values for Ti6Al4V, which were used in the current work, are available in the literature [7]. The intensity of the beam with a Gaussian

Table 2

Thermophysical properties of Ti6Al4V [29–31].

Property	Symbol	Value
Density	ρ	4,420 kg/m ³
Specific heat	c	$c = (0.176T + 540) \text{ J/kgC}$ $T \leq T_m$
		$c = 830.4 \text{ J/kgC}$ $T > T_m$
Thermal conductivity	k	$k = (0.0156T + 7) \text{ W/mC}$ $T \leq T_m$
		$k = 32.74 \text{ W/mC}$ $T > T_m$
Latent heat	L	418,680 J/kg
Melt temperature	T_m	1650 °C
Boiling temperature	T_b	3290 °C
Dynamic viscosity	μ	$5.2 \times 10^{-3} \text{ N s/m}^2$

distribution may be expressed as [28]

$$P(x, y, t) = P_0 h(t) e^{-[2r^2/r_b^2]} \quad (11)$$

where $r = \sqrt{x^2 + y^2}$ is the measured distance from the laser beam center and P_0 is the laser intensity at the center of the beam, which is defined as,

$$P_0 = \frac{2P_{\text{tot}}}{\pi r_b^2} \quad (12)$$

where r_b is the laser beam radius, P_{tot} is the total absorbed power, $P_{\text{tot}} = \eta P_{\text{incident}}$, P_{incident} is the incident laser power and η is the average absorptivity of the workpiece material. In Eq. (11), $h(t)$ shows the temporal variation of intensity. In the pulsed laser welding, when the pulse is active, the value of $h(t)$ is equal to 1 and when the pulse is inactive $h(t)$, it is equal to zero. The frequency of the welding determined the number of time steps that the pulse was on. The average absorptivity of Ti6Al4V plate workpiece is 0.34 [7]. Thermophysical properties of Ti6Al4V are shown in Table 2.

4. Results and discussion

According to the previous studies, the most important parameters that affect the welding processes are maximum temperature, the cooling rate, the welding speed, the pulse duration and the temperature gradient. In Fig. 3, the temperature histories for specific points (A and B) representing the positions of thermocouples have been plotted. In the experiment corresponding to this figure, the temperature histories of welding process were studied with the variation in the welding speed by keeping the remaining parameters equal to each other. It should be noted that the thermocouple delay time test measurements have been performed using experiments on the plate with the specified temperature. We concluded that the difference between the actual time and the time recorded with the thermocouple was 5.5 s. Hence we shifted all the experimental data to 5.5 s.

As shown in this figure, the finite volume (FV) thermal model (numerical simulation) was in good agreement with the experimental data. Also, we observed that the temperature histories for different welding speeds had similar trends in the case of identical welding speed. It can be observed that the temperature histories of both the numerical and experimental data had similar shapes when they were compared. This figure show that by decreasing the welding speed, the peak value of temperature diagram is increased and its maximum value occurs at a longer time.

It has been shown that the surface tension plays a key role in the fluid flow in a molten pool. Fluid flows from zones with the smaller surface tension towards zones with larger one. Also, the higher temperature leads to the smaller surface tension. Due to a relatively lower temperature at the edge of the molten pool, the surface tension turns out to be very large [32]. Hence, at the low

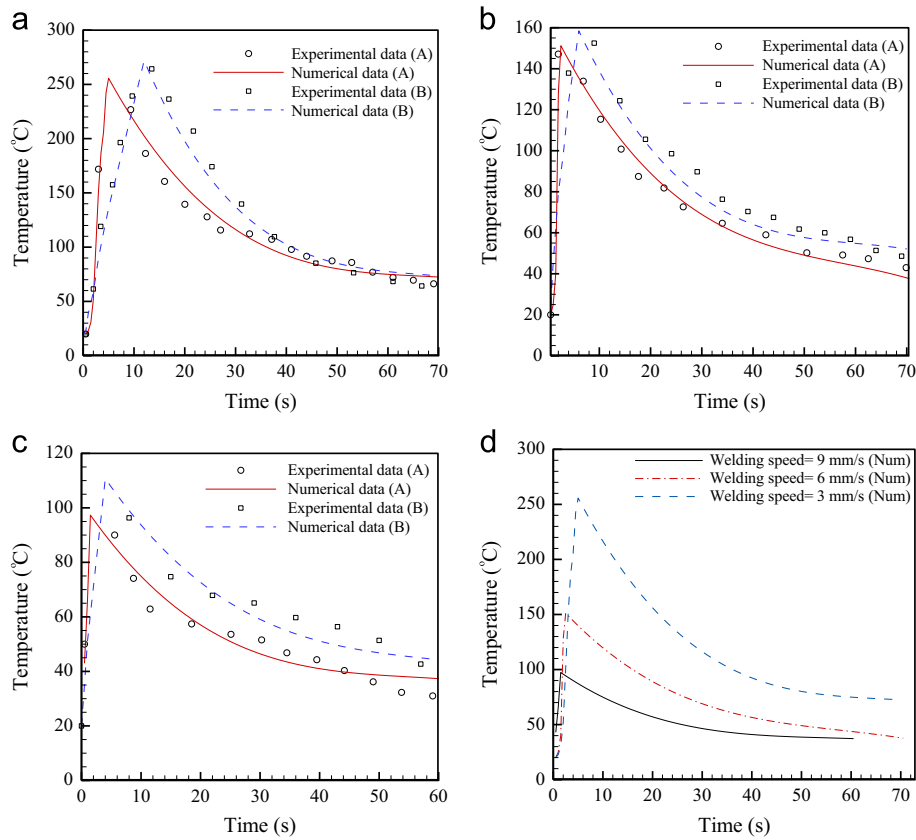


Fig. 3. Simulated and experimental results of temperature distribution for points A and B as a function of welding speed (a) $v=3$ mm/s, (b) $v=6$ mm/s, (c) $v=9$ mm/s and (d) all welding speeds for point A.

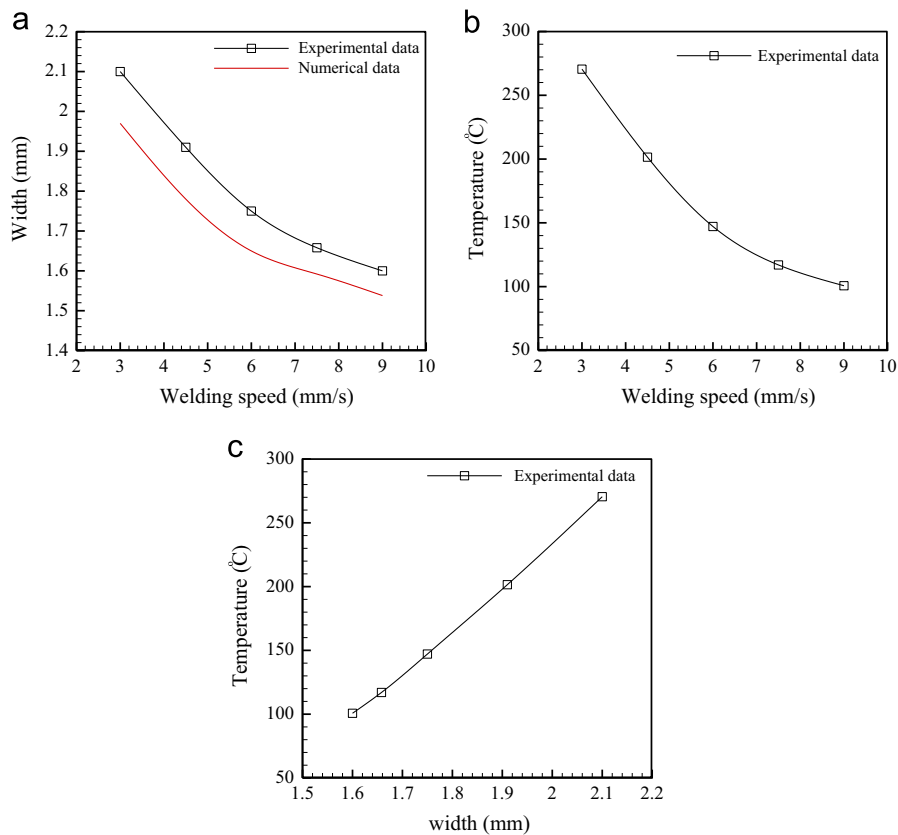


Fig. 4. Experimental results (point A): (a) width versus welding speed, (b) temperature distribution versus welding speed and (c) temperature distribution versus width.

welding speeds, the fluid velocity gets higher as it approaches the pool edges, relative to low fluid velocities in the pool center. Finally, heat is transferred to the surrounding as a result of fluid flow.

Fig. 4a reports the welding width versus welding speed achieved by performing an experimental setup with 25 Hz pulse frequency, 4.2 ms pulse duration and average power of 240 W. The welding speed was varied between 3 and 9 mm/s. According to our results, the width was decreased with increasing laser welding speed. This increase in the welding speed has an inverse effect on the welding width. In laser welding, a good weld is not only a weld with sufficient penetration but also, it is one with an acceptable weld surface (width). Hence from this figure, we can conclude that at sufficient low welding speed, we have a larger width and the weld surface has an acceptable quality. It should be noted that the numerical results agreed with the experimental data. The influence of the welding speed on the temperature (at experimental point 2 mm from the center of the melt pool) is shown in Fig. 4b. We can see that the temperature was decreased with increasing the welding speed. By combining Fig. 4a and b, we can obtain the graph of temperature versus the width of the weld pool (Fig. 4c). The obtain results predicted a smaller width in smaller temperature. This trend can be reasonable.

In the second series of experiments, variation of welding depth with welding speed in constant power was investigated. According to the experimental results discussed in Fig. 4, the laser pulse parameters selected were 240 W average power, 4.2 ms pulse duration and 25 Hz pulse frequency. Fig. 5a shows the melt pool depth as a function of welding speed. It is clearly seen that the melt pool depth was decreased by increasing the laser welding speed. This means that we observed that at a given laser power, a larger welding speed did produce lower penetration depth. In laser welding, the increase in welding speed and constant power results in a lower heating time not high enough to produce

significant penetration depth. It should be noted that at high welding speeds, the numerical results agreed with the experimental data. Also, because of the increase of the absorptivity at the lower speeds, the penetration depth evolution lightly disagreed with the experiment. This increase was the result of the multi reflection of the beam inside the keyhole [23]. Indeed, at lower welding speeds, a longer interaction time occurred between the incident laser beam and the base metal, causing the formation of a keyhole [17]. The influence of the welding speed on the temperature (at experimental point 2 mm from the center of the melt pool) is shown in Fig. 5b. As we observed in Fig. 4, by combining Fig. 5a and b, we can plot temperature versus penetration depth.

Fig. 6 shows the predicted temperature as a function of distance (from the laser beam center) at different laser welding speeds. It can be seen that at each welding speed, the temperature profile was decreased sharply close to the laser beam center and then decreased slightly in the far region from the laser beam center. Also, it can be observed that at each location, the temperature was decreased by increasing the welding speed. These high and low temperature gradients in the regions close and far from the melting pool are expectable. In the left side of the sample, there was convective heat transfer with the ambient fluid and in the right side, there was a melting pool. Based on the previous knowledge about heat transfer, we know that when there is convection heat transfer on the boundary of sample, the temperature profile approaches slightly to ambient temperature. This trend can be clearly observed in this figure.

The cross-sections of the welded samples were characterized using four geometric parameters. The first is called “ h_1 ” and it represents the width of HAZ. The second is called “ h_2 ” and it represents the penetration depth of the welding. The third is called “ h_3 ” and it represents the width of weld pool. These distances are shown in Fig. 7 [4].

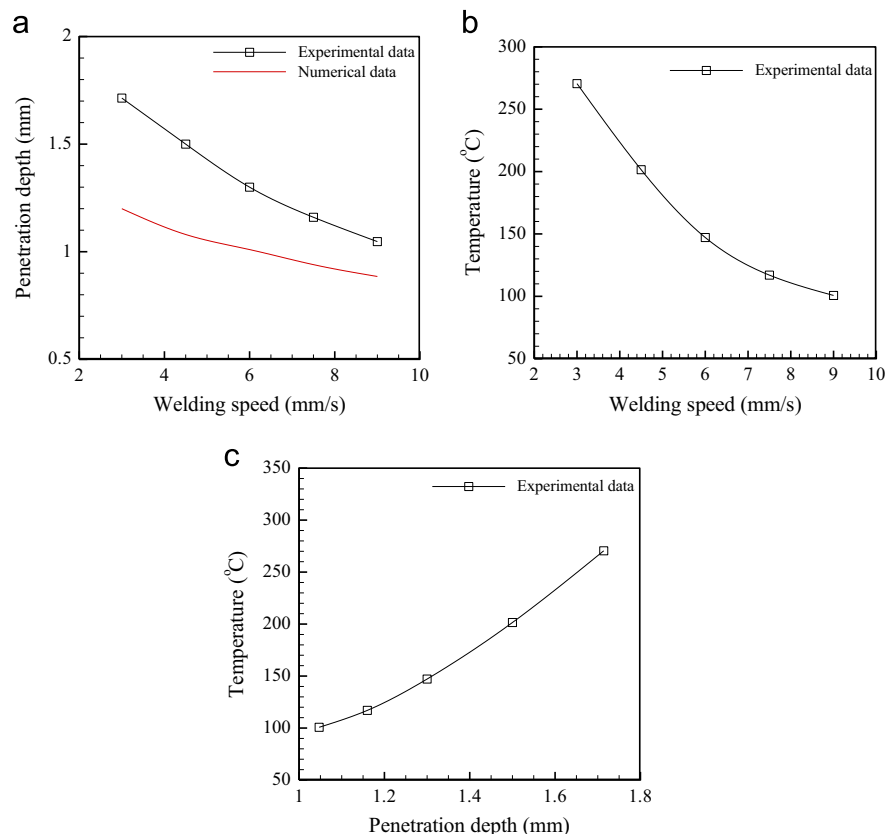


Fig. 5. Experimental results (point A): (a) depth versus welding speed, (b) temperature distribution versus welding speed and (c) temperature distribution versus depth.

Fig. 8 shows the cross sectional area of the samples according to parameters illustrated in Table 3. In Fig. 8, at lower welding speed, it was found that the penetration depth was increased at constant pulse duration and power. Also, the penetration depth

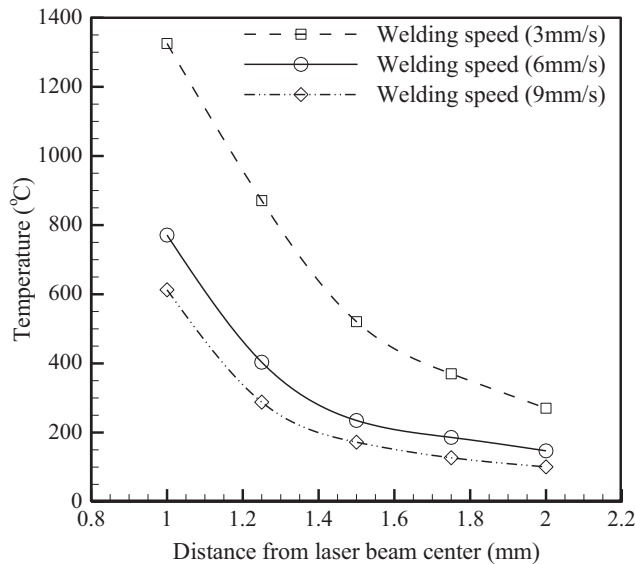


Fig. 6. Temperature distribution versus distance from laser beam center in different laser welding speed.

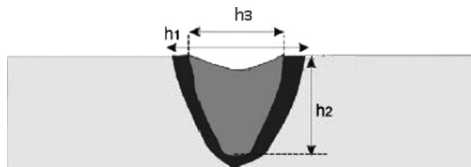


Fig. 7. Characterization of welding cross-section [4].

and HAZ were decreased by increasing the welding speed. This situation can be explained by the transfer of more heat energy (conduction) to keyhole walls with the decrease of speed. This presence of heat energy creates the deeper keyhole. Also, a numerically predicted temperature contour versus the experimental micrograph for welding speed of 3 mm/s is plotted in Fig. 8d for comparison between numerical and experimental results. It can be concluded that the predicted numerical temperature contours give a good insight related to phase transformation in the molten pool and HAZ as observed in Fig. 8d.

In this paper a numerical and experimental study of laser welding was conducted for prediction of temperature distribution and molten pool shape and HAZ dimensions. The variations in the weld geometry (width and depth) that affected by laser welding parameters indirectly estimated with considering the temperature variations around the molten pool which obtained from the numerical model. The finite volume thermal model is in good agreement with the experimental data. The model can predict the influences of laser welding speed on the weld pool shape and size related to temperature variations. The obtained results from the numerical model can help to better understanding of the mechanism of laser welding. The predicted numerical temperature contours give a good insight related to phase transformation in the molten pool and HAZ. The temperature measurement in appropriated distance from the molten pool that was conducted in the experiments can be useful for confirm the results obtained from finite volume model. The molten pool geometry (width and depth)

Table 3

The values of geometric parameters h_1 – h_3 at different laser welding speeds with mean laser power of 240 W, pulse duration of 4.2 ms and the frequency of 25 Hz.

Sample	Laser welding speed (mm/s)	h_1 (mm)	h_2 (mm)	h_3 (mm)
A	3	2.571	1.714	2.10
B	6	2.12	1.38	1.75
C	9	1.91	1.047	1.628

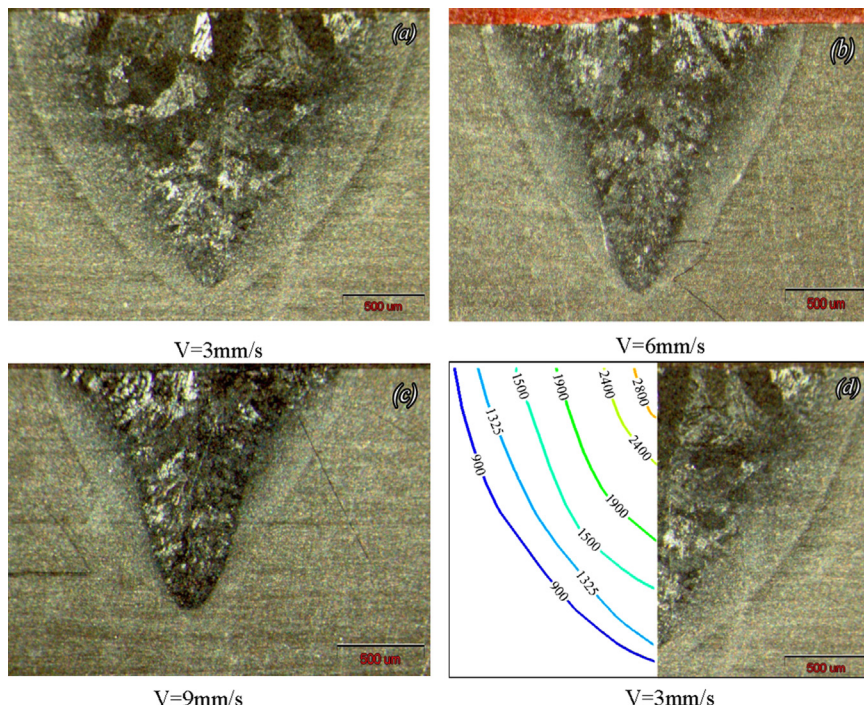


Fig. 8. The cross sectional area of the sample at different welding speeds; experimental results: (a) $v=3$ mm/s, (b) $v=6$ mm/s, (c) $v=9$ mm/s and comparison of the numerical and experimental results: (d) $v=3$ mm/s.

proportionally related to the welding speed as observed in numerical and experimental results. Increasing the welding speed reduces and decreasing the welding speed increases the width and depth of molten pool.

5. Conclusions

In this paper, a numerical and experimental study of laser welding for modeling temperature distribution was investigated to predict the depth and width of the molten pool and HAZ. The key findings and conclusions from the present simulation are as follows:

- The numerical simulation was in good agreement with the experimental data.
- The temperature histories for different welding speeds had similar trends and in the case of identical welding speed, it can be observed that the temperature histories of both the numerical and experimental data had similar shapes when they were compared.
- By decreasing the welding speed, the peak value of temperature diagram was increased and its maximum value occurred at a longer time.
- The width was decreased with increasing laser welding speed and at sufficient low welding speed, we had a larger width and the weld surface got acceptable quality.
- At each welding speed, the temperature profile was decreased sharply close to the laser beam center and then decreased slightly in the far region from the laser beam center.
- At lower welding speed, it was found that the penetration depth was increased at constant pulse duration, pulse frequency and power.

According to the obtained results of this study, estimation of the variations in the weld geometry (width and depth) could be done by considering the temperature variations around the molten pool. The results obtained from the model were precisely confirmed by the experimental data and can be used to predict indirectly molten pool geometry. By controlling the temperature and pulsed laser process parameters, it is possible to precisely control the welding process. Indeed, using the model can minimize the costs of experiments.

References

- [1] Mackwooda AP, Crafer RC. Thermal modelling of laser welding and related processes: a literature review. *Opt Laser Technol* 2005;37:99–115.
- [2] Wang SH, Wei MD, Tsay LW. Tensile properties of LBW welds in Ti–6Al–4V alloy at evaluated temperatures below 450 °C. *Mater Lett* 2003;57:1815–23.
- [3] Casalino G, Curcio F, Memola F, Minutolo C. Investigation on Ti6Al4V laser welding using statistical and Taguchi approaches. *J Mater Process Technol* 2005;167:422–8.
- [4] Akman E, Demir A, Canel T, Sinmazcelik T. Laser welding of Ti6Al4V titanium alloys. *J Mater Process Technol* 2009;209:3705–13.
- [5] Blackburn JE, Allen CM, Hilton PA, Li L, Hoque MI, Khan AH. Modulated Nd:YAG laser welding of Ti–6Al–4V. *Sci Technol Weld Joining* 2010;15:433–40.
- [6] Gao XL, Zhang LJ, Liu J, Zhang JX. A comparative study of pulsed Nd:YAG laser welding and TIG welding of thin Ti6Al4V titanium alloy plate. *Mater Sci Eng, A* 2013;559:14–21.
- [7] Yang J, Sun S, Brandt M, Yan W. Experimental investigation and 3D finite element prediction of the heat affected zone during laser assisted machining of Ti6Al4V alloy. *J Mater Process Technol* 2010;210:2215–22.
- [8] Kong F, Ma J, Kovacevic R. Numerical and experimental study of thermally induced residual stress in the hybrid laser–GMA welding process. *J Mater Process Technol* 2011;211:1102–11.
- [9] Frewin MR, Scott DA. Finite element model of pulsed laser welding. *Weld J* 1999;78:15s–22s.
- [10] Semak VV, Damkroger B, Kempka S. Temporal evolution of the temperature field in the beam interaction zone during laser material processing. *J Phys D: Appl Phys* 1999;32:1819–25.
- [11] Semak VV, Steele RJ, Fuerschbach PW, Damkroger BK. Role of beam absorption in plasma during laser welding. *J Phys D: Appl Phys* 2000;33:1179–85.
- [12] Spina R, Tricarico L, Basile G, Sibillano T. Thermo-mechanical modeling of laser welding of AA5083 sheets. *J Mater Process Technol* 2007;191:215–9.
- [13] Kong F, Santhanakrishnan S, Lin D, Kovacevic R. Modeling of temperature field and grain growth of a dual phase steel DP980 in direct diode laser heat treatment. *J Mater Process Technol* 2009;209:5996–6003.
- [14] Bannour S, Abderrazak K, Mhiri H, Palec GL. Effects of temperature-dependent material properties and shielding gas on molten pool formation during continuous laser welding of AZ91 magnesium alloy. *Opt Laser Technol* 2012;44:2459–68.
- [15] Fortunato A, Ascari A, Orazi L, Cuccolini G, Campana G, Tani G. Numerical simulation of nanosecond pulsed laser welding of eutectoid steel components. *Opt Laser Technol* 2012;44:1999–2003.
- [16] Assuncao E, Williams S. Comparison of continuous wave and pulsed wave laser welding effects. *Opt Lasers Eng* 2013;51:674–80.
- [17] Zervaki AD, Haidemenopoulos GN, Lambrakos SG. Inverse thermal analysis of heat-affected zone in Al2129 and Al2198 laser welds. *J Mater Eng Perform* 2013;22:1582–92.
- [18] Çam G, Koçak M. Progress in joining of advanced materials. *Int Mater Rev* 1998;43:1–44.
- [19] Çam G, Koçak M. Progress in joining of advanced materials—Part I: Solid state joining, fusion joining, and joining of intermetallics. *Sci Technol Weld Joining* 1998;3:105–26.
- [20] dos Santos J, Çam G, Torster F, Insfran A, Riekehr S, Ventzke V, et al. Properties of pbeam welded steels, Al- and Ti-alloys: significance of strength mismatch. *Weld World* 2000;44:42–64.
- [21] Çam G, Koçak M, dos Santos JF. Developments in laser welding of metallic materials and characterization of the joints. *Weld World* 1999;43:13–26.
- [22] Patankar SV, Spalding DB. A calculation procedure for heat, mass and momentum transfer in three-dimensional parabolic flows. *Int J Heat Mass Transfer* 1972;15:1787–806.
- [23] Abderrazak K, Bannour S, Mhiri H, Lepalec G, Autric M. Numerical and experimental study of molten pool formation during continuous laser welding of AZ91 magnesium alloy. *Comput Mater Sci* 2009;44(3):858–66.
- [24] Bennon WD, Incropera FP. A continuum model for momentum, heat and species transport in binary solid–liquid phase change systems—I model formulation. *Int J Heat Mass Transfer* 1987;30(10):2161–70.
- [25] Voller VR, Prakash C. A fixed grid numerical modeling methodology for convection diffusion mushy region phase-change problems. *Int J Heat Mass Transfer* 1987;30:1709–19.
- [26] Ha EJ, Kim WS. A study of low-power density laser welding process with evolution of free surface. *Int J Heat Fluid Flow* 2005;26:613–21.
- [27] Fan HG, Tsai HL, Na SJ. Heat transfer and fluid flow in a partially or fully penetrated weld pool in gas tungsten arc welding. *Int J Heat Mass Transfer* 2001;44:417–28.
- [28] Singh R, Alberts MJ, Melkote SN. Characterization and prediction of the heat-affected zone in a laser-assisted mechanical micromachining process. *Int J Mach Tools Manuf* 2008;48:994–1004.
- [29] Bolz RE, Tuve GL. CRC handbook of tables for applied engineering science. Boca Raton, FL: CRC Press; 1973.
- [30] Mills KC. Recommended thermophysical properties for selected commercial alloys. Cambridge (England): Woodhead Publishing; 2002.
- [31] Smithells CJ. Smithell's metals reference book. Heinemann: Boston (MA): Elsevier Butterworth; 2004.
- [32] Li Y, Feng YH, Zhang XX, Wu CS. An improved simulation of heat transfer and fluid flow in plasma arc welding with modified heat source model. *Int J Therm Sci* 2013;64:93–104.